

Article

Fabrication of Zinc Protoporphyrin-Modified Gold Electrode for Sensitive and Fast Detection of Vascular Endothelial Growth Factor

Hung-Yu Lin ^{1,2,3}, Chin-Cheng Liao ^{1,2,3} and Mu-Yi Hua ^{1,2,3,4,*}

¹ Department of Chemical and Materials Engineering, Chang Gung University, Taoyuan 333323, Taiwan; zcbm8217@gmail.com (H.-Y.L.); williamliao085@yahoo.com.tw (C.-C.L.)

² Biomedical Engineering Research Center, Chang Gung University, Taoyuan 333323, Taiwan

³ Healthy Aging Research Center, Chang Gung University, Taoyuan 333323, Taiwan

⁴ Department of Gastroenterology and Hepatology, Linkou Chang Gung Memorial Hospital, Taoyuan 333423, Taiwan

* Correspondence: huamy@mail.cgu.edu.tw; Tel.: +886-3-2118800#5289

Abstract: Vascular endothelial growth factor (VEGF) is directly related to cancer growth and its distant spread, and thus, it is considered a promising biomarker for diagnosis and post-treatment monitoring of patients with malignancies. Zinc protoporphyrin (ZnPP) is a zinc-centered raw purple compound (protoporphyrin) that has unique optical and electrochemical characteristics. In this study, we used a ZnPP-modified gold electrode to generate a chemical bond with Avastin by self-assembly and fabricate a Au/ZnPP/Avastin electrode. Bovine serum protein (BSA) was added to the electrode to prevent non-specific linkage with biomolecules. The prepared Au/ZnPP/Avastin/BSA electrodes were used for the detection of VEGF by cyclic voltammetry and amperometry. The optical properties of ZnPP were analyzed with an ultraviolet/visible/near-infrared spectrometer and a photoluminescence spectrometer. The structural and hydrophilic/hydrophobic properties of the ZnPP-modified gold electrodes were investigated by Fourier-transform infrared spectroscopy and contact angle gauge, respectively. VEGF was detected with the Au/ZnPP/Avastin/BSA electrodes prepared either with (w/LT) or without light treatment (w/o LT). The w/LT electrode showed a linear range and a sensitivity of 0.1 pg/mL–10 ng/mL and 6.52 $\mu\text{A}/\log(\text{pg/mL})\text{-cm}^2$, respectively; the corresponding values for the w/o LT electrode were 10 pg/mL–10 ng/mL and 3.15 $\mu\text{A}/\log(\text{pg/mL})\text{-cm}^2$, respectively. The w/LT electrode had good specificity for VEGF and was minimally influenced by other molecules. The excellent detection range, high sensitivity, and high selectivity for VEGF detection indicate that Au/ZnPP/Avastin electrodes have great potential for diagnostic and prognostic applications in patients with malignancies.

Keywords: vascular endothelial growth factor; Avastin; zinc protoporphyrin; light treatment; modified Au electrode; cyclic voltammetry; amperometry



Citation: Lin, H.-Y.; Liao, C.-C.; Hua, M.-Y. Fabrication of Zinc Protoporphyrin-Modified Gold Electrode for Sensitive and Fast Detection of Vascular Endothelial Growth Factor. *Chemosensors* **2021**, *9*, 21. <https://doi.org/10.3390/chemosensors9020021>

Received: 20 December 2020

Accepted: 20 January 2021

Published: 23 January 2021

Publisher's Note: MDPI stays neutral with regard to jurisdictional claims in published maps and institutional affiliations.



Copyright: © 2021 by the authors. Licensee MDPI, Basel, Switzerland. This article is an open access article distributed under the terms and conditions of the Creative Commons Attribution (CC BY) license (<https://creativecommons.org/licenses/by/4.0/>).

1. Introduction

Protoporphyrin and its derivatives are widely distributed macromolecules that contain hemoglobin, collagen, and vitamin B12 [1]. Zinc protoporphyrin (ZnPP) is a macrocycle that consists of four pyrrole units for the tower, four methylene units for the bridge, and metal zinc chelate, ultimately resulting in a ring structure [2]. Because ZnPP has a multi-electron resonance structure that can be excited at a specific wavelength, ZnPP films can be used to monitor the energy transfer between electrons during fluorescence [3]. Its unique structure and optical properties have been confirmed by ultraviolet/visible (UV/Vis)/near-infrared (IR), Fourier-transform IR (FTIR), and photoluminescence (PL) [4].

Vascular endothelial growth factor (VEGF) is a heparin-binding growth factor that acts as a master regulator of angiogenesis, i.e., the formation of new blood vessels. VEGF

is known to be released in large amounts by cancer cells to increase their blood supply. Accordingly, the growth and spread of solid tumors is critically dependent on the presence of adequate vascular networks. In this regard, VEGF has been shown to promote the viability of cancer cells [5,6] and is frequently overexpressed in solid malignancies [7]. An increase in serum VEGF levels has been reported in clinical populations affected by different tumors [5,8,9]. Avastin—a monoclonal antibody against VEGF—has been shown to block tumor-associated angiogenesis. The reduced oxygen and nutrient supply resulting from angiogenesis blockade eventually induces apoptosis of malignant cells [10]. Accumulating evidence indicates that Avastin exerts its anti-angiogenic effects by competing with the VEGF receptor for VEGF binding [11–13]. In clinical practice, Avastin is extensively applied for the treatment of diabetic retinopathy—a condition characterized by excess retinal angiogenesis [14]. Herein, we used Avastin as a primary antibody for VEGF detection owing to its affinity for this angiogenic growth factor.

Photoelectrochemical biosensors have been the subject of intense research interest [15–18]. Li and coworkers have focused on miRNA [19,20], whereas Chen and colleagues were able to develop photoelectrochemical biosensors for the detection of nucleic acids [21]. Other photoelectrochemical biosensors have been developed for detecting tyrosine [22] and adenosine triphosphate in cancer cell extracts [23]. Additionally, we have previously investigated protein detection using polycrystalline-silicon nanowire field-effect transistors [8,24].

In this study, we fabricated Au/ZnPP/Avastin electrodes by taking advantage of the specific binding between VEGF and Avastin (a monoclonal antibody against VEGF). Additionally, Avastin was immobilized on the Au/ZnPP electrodes through the interaction between the zinc ions of ZnPP and the lone pair electrons of nitrogen atoms in the antibody. Bovine serum protein (BSA) was added to prevent non-specific binding to the electrode [24,25]. The Au/ZnPP/Avastin/BSA electrodes prepared in this study were used to measure VEGF concentrations by cyclic voltammetry (CV) and amperometry. According to Ohm's law, biological macromolecules such as monoclonal antibodies have poor conductivity; thus, Avastin binding yields to a decreased current. VEGF concentrations as detected by the Au/ZnPP/Avastin/BSA electrodes were quantified by measuring the current variation before and after VEGF binding.

2. Materials and Methods

2.1. Reagents

ZnPP was obtained from Alfa Aesar; N-methyl-2-pyrrolidone (NMP), potassium ferricyanide ($K_3Fe(CN)_6$), and potassium ferrocyanide ($K_4Fe(CN)_6$) were purchased from Merck; L-cysteine, human serum albumin (HSA), human immunoglobulin G (IgG) antibodies, and creatinine were from Sigma-Aldrich; BSA was obtained from Elabscience (BSA (E-IR-R108)); Avastin was from F. Hoffmann-La Roche; and vascular endothelial growth factor (VEGF) was obtained from Abcam (recombinant human VEGF-A protein (ab155740)).

2.2. Characterizations of ZnPP

The optical properties of ZnPP in liquid and solid states were analyzed using UV/Vis and near-IR spectroscopy (JASCO V-650) at wavelengths of 190–900 nm for absorption spectral analysis. A total of 15.6 $\mu\text{g/mL}$ of a ZnPP/NMP solution was prepared by dissolving ZnPP in NMP and subsequently placed in quartz cells for analysis. Solid ZnPP films were prepared by coating a ZnPP/NMP solution on a quartz sheet, which was subsequently vacuum-dried. FTIR spectroscopy (Bruker Tensor 27 FTIR spectrometer) and enzyme-linked immunosorbent assay (ELISA) were used to verify self-assembly of ZnPP with an amino acid (e.g., cysteine) and proteins. In FTIR testing, samples were analyzed with a resolution of 8 cm^{-1} at wavenumbers of 4000–400 cm^{-1} ; 2 mg/mL ZnPP/NMP solution and 3.3 mg/mL cysteine aqueous solution were mixed and shocked in a volume ratio of 5:3 for 3 h before being centrifuged. After centrifugation, the sediment was vacuum-dried for 180 min to obtain the ZnPP/cysteine (ZnPP/cys) compound. ZnPP, cysteine, and ZnPP/cys

were homogenized with KBr powder and analyzed using a Bruker Tensor 27 FTIR spectrometer after molding with oil pressing equipment and abrasives. The PL intensities of the 2.5 µg/mL ZnPP/NMP solutions at wavelengths of 300–800 nm were measured using excitation light (wavelength: 430 nm) using a PerkinElmer LS55 PL spectrometer. The hydrophobic/hydrophobic properties of the Au/ZnPP and Au/ZnPP/Avastin electrodes were measured with a contact angle gauge (type 22AUC03; manufacturer: FTA). The light absorption densities of the Au/ZnPP electrodes were measured using the Bradford method either with or without light treatment (w/LT and w/o LT, respectively) using a white-light lamp (1200 lm) for 20 min. The Bradford solution was prepared by dissolving 50 mg Coomassie blue (g250; ACROS ORGANICS) into 50 mL methanol. Subsequently, 100 mL 85% of phosphoric acid (H₃PO₄) and 850 mL DI water were concomitantly added, stirred for 30 min, and stored at 4 °C. We then added 0.136 mg/mL of BSA protein droplets to the w/LT and w/o LT Au/ZnPP electrodes. BSA solutions were removed and incubated with Coomassie blue (g250) at 37 °C for 30 min. Finally, the light absorption densities (wavelength: 595 nm) were measured with ELISA.

2.3. Fabrication of VEGF Biosensors with and without Light Treatment

The production process of the VEGF sensing electrodes is shown in Figure 1. In an effort to optimize both Avastin and BSA concentrations, we used differential pulse voltammetry (DPV) to measure the differences in the current before and after the addition of Avastin and BSA on the Au/ZnPP electrode. First, 2.5 µL of 5.0 × 10⁻³ wt% (440 µg/mL) ZnPP/THF solution were coated on a Au electrode at 50 °C for 3 min as a Au/ZnPP electrode. The Au/ZnPP electrode was subsequently incubated with 20 µL of 1.25 mg/mL, 125 µg/mL, 31.25 µg/mL, 12.5 µg/mL, and 1.25 µg/mL of Avastin, respectively, for 1.5 h to immobilize the Au/ZnPP electrode as Au/ZnPP/Avastin. Upon calculating the current difference between Au/ZnPP and Au/ZnPP/Avastin electrodes, we identified the electrode with 31.25 µg/mL of Avastin as that having the highest stability. In an effort to increase the specificity of the Au/ZnPP/Avastin electrode for VEGF, we used BSA as a blocking buffer. The optimized Au/ZnPP/Avastin electrode was incubated with 20 µL of 1.36 mg/mL, 136 µg/mL, 62.5 µg/mL, and 13.6 µg/mL of BSA, respectively, for 1 h to immobilize the Au/ZnPP/Avastin electrode as a Au/ZnPP/Avastin/BSA electrode. The DPV results revealed that 136 µg/mL of BSA led to blocking buffer saturation. Owing to the limited electrode area, the addition of excess BSA would result in a decreased current. Therefore, an optimized BSA concentration (136 µg/mL) was used for preparation of the Au/ZnPP/Avastin/BSA electrodes (w/o LT). For comparison purposes, the Au/ZnPP/Avastin/BSA electrodes with light treatment (w/LT) were also prepared under the same optimized conditions. Owing to their stability and limited cost, BSA and milk are frequently used as blocking agents to avoid non-specific reactions [26,27]. Thus, the Au/ZnPP electrode was initially treated with 200 µL of 0.01 M PBS solution before conducting amperometry experiments (960 s at 0.38 V). The 1200 lm white-light lamp treatment was started at 60 s, and 20 µL of Avastin was added at 31.25 µg/mL at 360 s to fix the Avastin to the Au/ZnPP electrode and form the Au/ZnPP/Avastin electrode (w/LT). Subsequently, 0.136 mg/mL BSA was added to Au/ZnPP/Avastin electrodes (w/LT) to produce Au/ZnPP/Avastin/BSA electrodes (w/LT). Image analyses of the electrode surface and of Zn atoms distribution were carried out using field-emission scanning electron microscopy (FESEM-Hitachi SU8010, Georgia Institute of Technology, Atlanta, GA, USA) and energy-dispersive X-ray spectroscopy (EDX, Bruker xflash detector 5030, Bruker AXS GmbH, Karlsruhe, Germany), respectively.

2.4. Detection of VEGF and Selectivity Tests

Different concentrations of VEGF were added to Au/ZnPP/Avastin/BSA electrodes (w/LT and w/o LT), which underwent incubation for 1 h at 4 °C. Unbound VEGF was washed off with deionized (DI) water. The current changes in the electrodes were measured using amperometry in a 20 mM K₃Fe(CN)₆/K₄Fe(CN)₆ solution. Specificity tests for

Au/ZnPP/Avastin/BSA electrodes (w/LT) were conducted by adding VEGF (10 ng/mL), human serum albumin (HSA, 6.57 ng/mL), IgG antibody (1.0 mg/mL), and creatinine (6.0 mg/mL), respectively. We also tested a mixture consisting of VEGF (10 ng/mL), IgG antibody (0.45 mg/mL), and HAS (2.95 mg/mL) to mimic the conditions found in human serum. The above molecules were washed off with DI water after 1 h of reaction, and the current changes were measured using amperometry with a 20 mM $K_3Fe(CN)_6/K_4Fe(CN)_6$ solution.

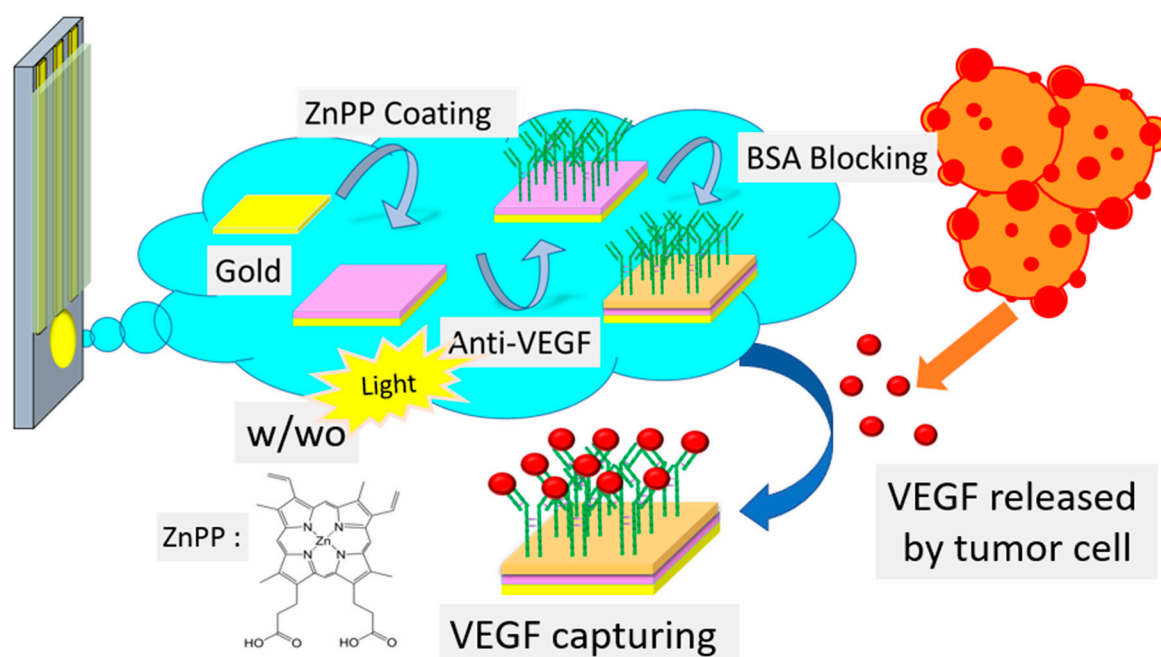


Figure 1. Schematic of Au/ZnPP/Avastin/bovine serum protein (BSA) with or without light treatment (w/LT and w/o LT) electrode preparation process.

3. Results and Discussion

3.1. FESEM Image and EDX Mapping

FESEM images of Au, Au/ZnPP, and Au/ZnPP/Avastin electrodes and EDX mappings of zinc atoms on Au/ZnPP and Au/ZnPP/Avastin electrodes are shown in Figure 2. The surface of the Au electrode was found to be flat and uniform, with obvious crystal boundaries (Figure 2a). Modification of ZnPP in the Au/ZnPP electrode resulted in an increased roughness of the electrode surface with holes of different sizes; this phenomenon may have been caused by THF volatilization when the ZnPP/THF solution was vacuum-dried into a film (Figure 2b). When the Au/ZnPP electrode was bound with Avastin, the aggregated structure appeared more evident on the Au/ZnPP/Avastin electrode surface. This may occur as a result of Avastin having keys knotted on the Au/ZnPP electrode surface. On comparing the content of Zn atoms on electrode surfaces, we found that the Zn content of the Au/ZnPP/Avastin electrode was lower than that observed for the Au/ZnPP electrode (Figure 2d–f). This observation can be explained by the presence of Avastin on the Au/ZnPP electrode surface, which may hamper the detection of Zn content. The roughness and Zn content of the electrode surface point to the presence of a successful key knot of Avastin on the Au/ZnPP/Avastin electrode.

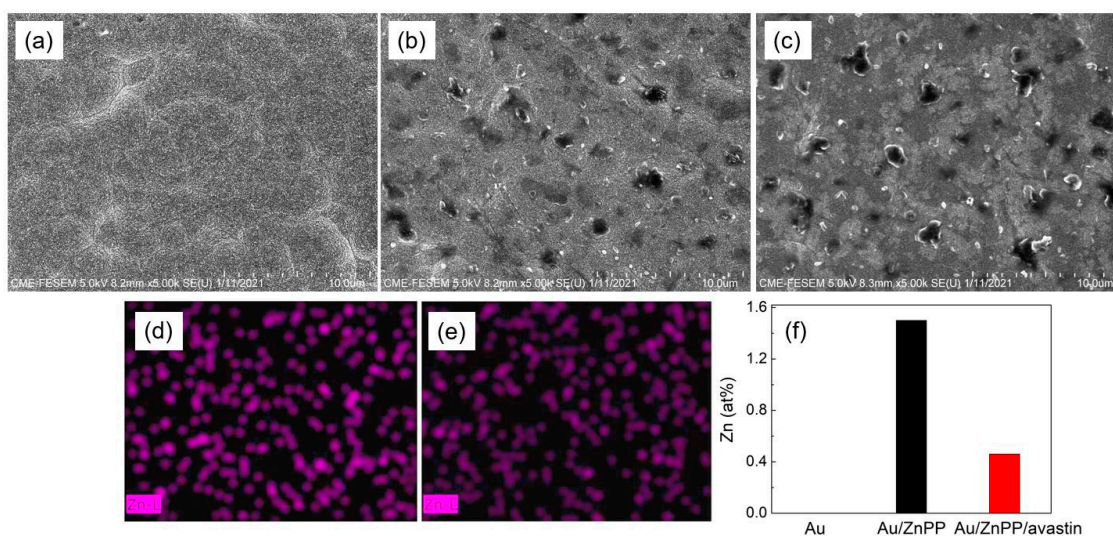


Figure 2. Images of the (a) Au electrode, (b) Au/ZnPP electrode, (c) Au/ZnPP/Avastin electrode and the energy-dispersive X-ray spectroscopy (EDX) mappings of zinc atom on (d) Au/ZnPP electrode, and (e) Au/ZnPP/Avastin electrode. Percentage of zinc atoms on the Au/ZnPP and Au/ZnPP/Avastin electrodes (f). The field-emission scanning electron microscopy (FESEM) and EDX scales are 5000 \times .

3.2. UV/Vis Near-IR and PL Spectroscopy FESEM Image

Figure 3 shows the UV/Vis near-IR spectra of the ZnPP/NMP solution (color: dark fuchsia). From Figure 3a,b, it can be seen that ZnPP/NMP has three main peaks at 423, 549, and 589 nm. The strong peak at 423 nm corresponds to the strong absorption peaks of the π - π^* transition from the protoporphyrin structure of ZnPP (also known as B-band or Soret band). The remaining two peaks at 549 and 589 nm correspond to the transition of electrons between nitrogen atoms and zinc ions in the protoporphyrin structure (also known as Q-band) [27]. The absorption peaks of the ZnPP solid films are located at 416, and 557 and 599 nm [27]. On comparing the energy transition of the ZnPP/NMP solution with that of the ZnPP solid film, the B-band of the ZnPP solid film shifted from 423 to 416 nm, which was due to the occasional disappearance of the NMP polar solvent. This resulted in an increase in the energy required by the π - π^* transition and in a decreased wavelength of the blue shift for the B-band. In addition, the Q-band characteristic peak of the ZnPP solid film is broader than that of the liquid, increasing from 549 and 589 nm to 557 and 599 nm, respectively (corresponding to red shifts of 8 and 10 nm, respectively). This is caused by an increased coplanarity of protoporphyrin molecules after NMP vaporization from the ZnPP/NMP solution. In turn, this makes the electron transitions between nitrogen atoms and zinc ions in the ZnPP solid film occur with longer wavelengths (lower energy) [28]. In Figure 3c, two emission fluorescence peaks can be observed at 593 and 642 nm; this indicates that when the ZnPP/NMP solution is excited by 430 nm light, it emits fluorescence at 593 and 642 nm, respectively. Collectively, these findings demonstrate that the ZnPP/NMP solution has a significant light sensitivity [28].

3.3. FTIR Spectroscopy

Heme is a derivative of porphyrin which consists of iron ions surrounded by porphyrin rings. Hemoglobin, which consists of several hemes and amino acids, carries oxygen using the high adhesion of central iron ions and oxygen, while iron ions can also be combined to amino acids, such as histidine and cysteine [29]. To verify the relationship between ZnPP and biomolecules of the same porphyrin derivative, FTIR was used to determine the changes in the characteristic functional groups after the reaction of cysteine and ZnPP (ZnPP/cys). Figure 4 shows the FTIR spectra of cysteine, ZnPP, and ZnPP/cys. In Figure 4a, the characteristic peaks of cysteine can be observed at 3469 (O–H stretching vibration), 3176 (N–H stretching vibration), 2980 (mixed asymmetric and symmetric stretching vibration

of $-\text{CH}_2-$), 2551 (S–H stretching vibration), 2086 (N–H stretching vibration of $-\text{NH}_3^+$), 1600 (mixed C=O stretching vibration and N–H bending vibration), and 638 cm^{-1} (C–S stretching vibration) [12,13]. In Figure 4b, the characteristic peaks of ZnPP can be observed at 3433 (O–H stretching vibration), 2914 (asymmetric stretching vibration of $-\text{CH}_2-$), 2858 (symmetric stretching vibration of $-\text{CH}_2-$), 2360 (C=O stretching vibration of absorbed CO_2), and 1701 cm^{-1} (C=O stretching vibration of $-\text{COOH}$) [30,31]. In Figure 4c, the main characteristic peaks of ZnPP/cys can be observed at 3444 (O–H stretching vibration), 3030 (mixed N–H stretching vibration and asymmetric/symmetric stretching vibration of $-\text{CH}_2-$), 2586 (S–H stretching vibration), 2094 (N–H stretching vibration of $-\text{NH}_3^+$), 1714 (C=O stretching vibration of $-\text{COOH}$), 1585 (mixed C=O stretching vibration and N–H bending vibration), and 615 cm^{-1} (C–S stretching vibration) [30,31]. By comparing the FTIR absorption spectra of ZnPP/cys and ZnPP, the N–H stretching vibration shifts from 3176 cm^{-1} in cysteine toward a lower wavenumber of 3030 cm^{-1} in ZnPP/cys (mixed with the asymmetric and symmetric stretching vibration of $-\text{CH}_2-$), which is due to the formation of hydrogen bonds between the N–H stretching vibrations of cysteine and the $-\text{COOH}$ of ZnPP. This is confirmed by the fact that the wavenumber of the C=O stretching vibration (1714 cm^{-1}) of ZnPP/cys is higher than that of ZnPP (1701 cm^{-1}), and the wavenumber of the N–H stretching vibration of $-\text{NH}_3^+$ (2094 cm^{-1}) of ZnPP/cys is higher than that of cysteine (2086 cm^{-1}) [31,32]. Moreover, the wavenumber of the S–H stretching vibration (2586 cm^{-1}) of ZnPP/cys is higher than that of cysteine (2551 cm^{-1}), and the wavenumber of C–S stretching vibration (615 cm^{-1}) of ZnPP/cys is lower than that of cysteine (638 cm^{-1}); this is due to the interaction between the Zn^{2+} of ZnPP and the S atom of cysteine, which prevents the S–H stretching vibration and lowers its vibration energy [31,32]. From the above results, it is evident that ZnPP can self-assemble with cysteine perfectly.

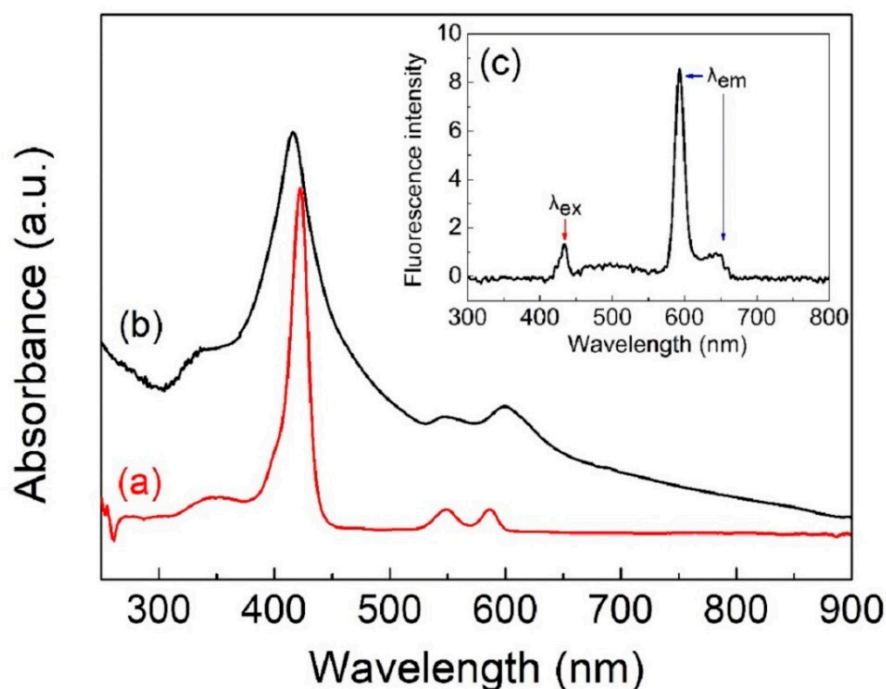


Figure 3. Ultraviolet/visible (UV/Vis) near-infrared (IR) spectra of (a) 156 ng/mL ZnPP/NMP solution and (b) ZnPP solid film; (c) photoluminescence (PL) spectrum of 2.43 ng/mL ZnPP/NMP solution.

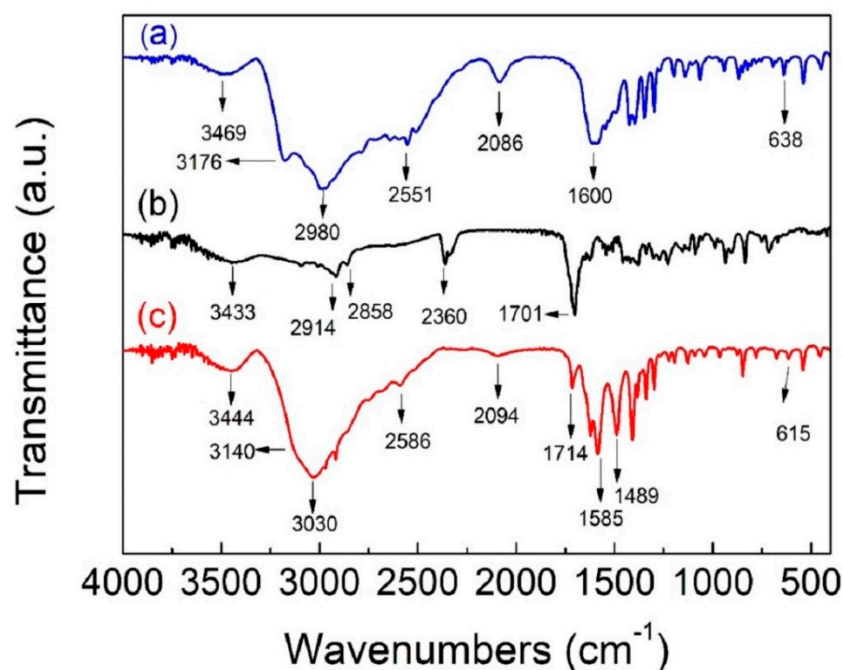


Figure 4. Fourier-transform IR (FTIR) spectra of (a) cysteine, (b) ZnPP, and (c) ZnPP/cys.

3.4. Electrochemical Phenomena of Au/ZnPP Electrodes with and without Light Treatment

The results reported in Figure 3 indicate that ZnPP can be stimulated by light and can induce an electron transition. Therefore, it is interesting to study and compare the electrochemical phenomena of Au/ZnPP electrodes with and without light treatment. The electrochemical performances of the Au/ZnPP electrodes (w/LT and w/o LT) were determined by CV and amperometry, and the results are shown in Figure 5. From Figure 5a, it is shown that the current of the w/o LT and w/LT electrodes stabilize at 910 and 990 μA (red line), respectively. Similar results were obtained by amperometry, as shown in Figure 5b. The current of both w/o LT and w/LT Au electrodes is approximately 65–75 μA (black line), while that of the Au/ZnPP electrode increases from 52 to 100 μA (blue line) in 500 s. When the light source is turned off, the current of the Au/ZnPP electrode decreases from 100 to 80 μA in 300 s, indicating that the Au/ZnPP electrode is significantly affected by light. This is because when ZnPP is stimulated by light, electrons transfer between ZnPP and the electrodes, which in turn produces optical currents [33–35].

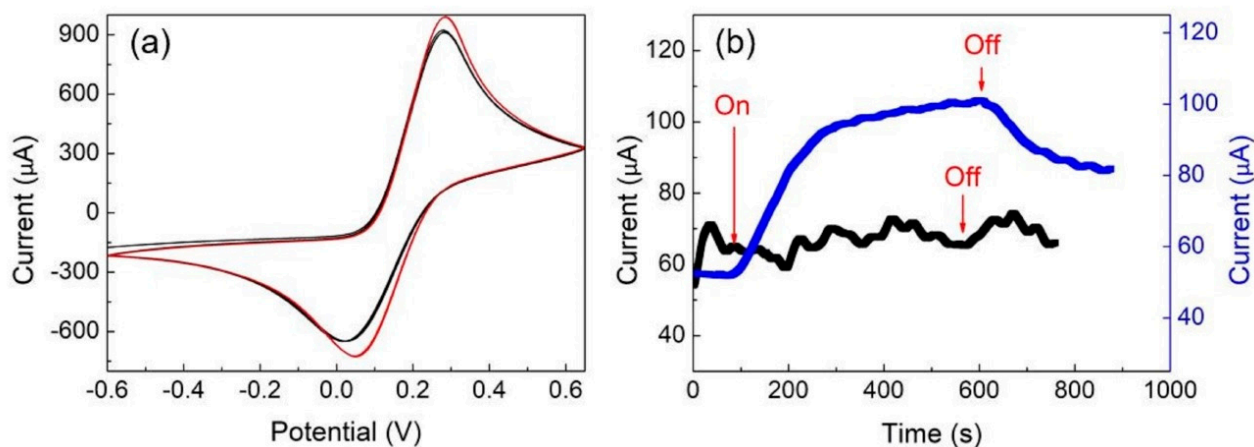


Figure 5. (a) Cyclic voltammetry (CV) spectra of Au/ZnPP electrodes without light exposure (black line) and with light exposure (red line). (b) Current-time diagram of Au (black lines) and Au/ZnPP electrodes (blue lines) following light treatment.

3.5. Contact Angles and Avastin Immobilization

The average contact angles ($n = 9$) of the Au/ZnPP (w/o LT), Au/ZnPP/Avastin (w/o LT), and Au/ZnPP/Avastin (w/LT) electrodes were 72.0° , 67.7° , and 51.5° , respectively, as shown in Figure 6. Figure 6 reveals that the surface of the Au/ZnPP electrode (w/o LT) has the worst hydrophilicity (Figure 6a), followed, in order, by the Au/ZnPP/Avastin electrode (w/o LT) (Figure 6b) and the Au/ZnPP/Avastin electrode (w/LT) (Figure 6c). This is due to the hydrophobicity of ZnPP and Avastin. When Avastin is bonded to the surface of the Au/ZnPP electrode, the contact angle becomes smaller. Meanwhile, the hydrophobicity of the Au/ZnPP/Avastin electrode (w/o LT) can be further decreased by light treatment, indicating that ZnPP stimulated by light can generate electron transfer and interaction between ZnPP and Avastin, which further increases the hydrophilicity of Avastin.

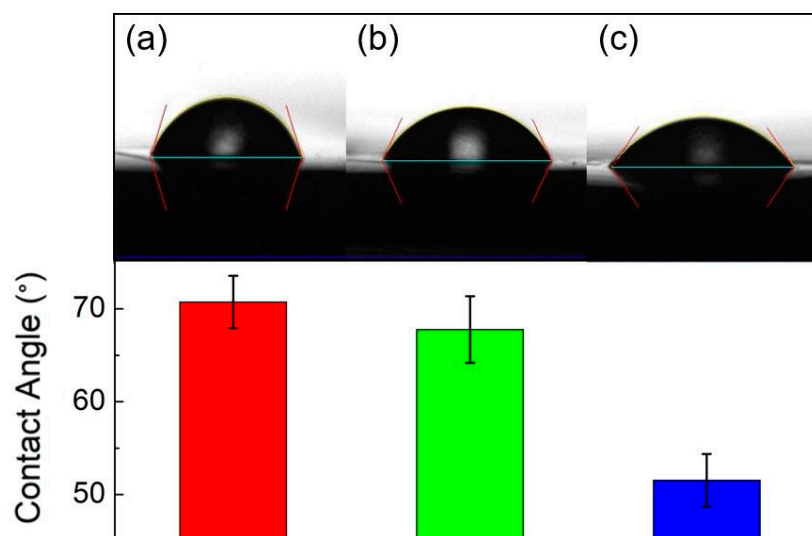


Figure 6. Contact angle of (a) Au/ZnPP electrode (w/o LT) and (b) Au/ZnPP/Avastin electrode (w/o LT), which were kept under dark conditions for 10 min, and (c) Au/ZnPP/Avastin electrode (w/LT), which was exposed to white light of 1200 lm for 10 min. Bars indicate the mean contact angle values ($n = 9$).

Coomassie blue (g250) is a dye that easily reacts with arginyl and lysyl residues [36–38]. The Bradford method involves reacting g250 with proteins to induce strong signal properties at 595 nm for protein quantification. To verify that the Au/ZnPP electrode interacts with protein molecules, 0.136 mg/mL of BSA protein droplets was placed on the Au/ZnPP electrodes (w/LT and w/o LT) for 2, 5, and 20 min. Then, the BSA liquid was collected, and its optical density was measured by ELISA. Figure 7 shows that the concentration and optical density (OD) of BSA under light treatment decrease gradually as the reaction time with Au/ZnPP increase, which indicates that the BSA key is complementary to ZnPP, proving that there is an interaction between ZnPP and BSA. After 20 min of reaction, the concentration of BSA with light treatment is markedly lower than that without light treatment, which proves that exposure to light increases the bonding between the Au/ZnPP electrodes and protein molecules.

To confirm the expected increase in the responsiveness of the Au/ZnPP electrode to Avastin under 1200 lm white light exposure, 31.25 $\mu\text{g/mL}$ of Avastin droplets was added to the Au/ZnPP electrodes (w/LT and w/o LT) for 10 min and to another Au/ZnPP electrode (w/o LT) for 1.5 h. Data were collected using amperometry. Figure 8 shows the differences in current between the Au/ZnPP/Avastin and Au/ZnPP electrodes (w/o LT) and between the Au/ZnPP/Avastin and Au/ZnPP electrodes (w/LT). After a reaction time of 10 min, the current drop in the w/o LT electrodes is 26.3 μA (Figure 8a), which is much larger than that in the w/o LT electrodes (4 μA , see Figure 8b). Even after a reaction time of 1.5 h without light exposure, the current drop is only 7 μA (Figure 8c). According to Ohm's law,

the drop in current is positively correlated to the increase in resistance. Under the current experimental conditions, this reflects an increase in the concentration of Avastin bound to the Au/ZnPP electrode (w/LT). Collectively, these results indicated that exposure to light with a luminous flux of 1200 lm significantly increased the reactivity of Au/ZnPP with Avastin.

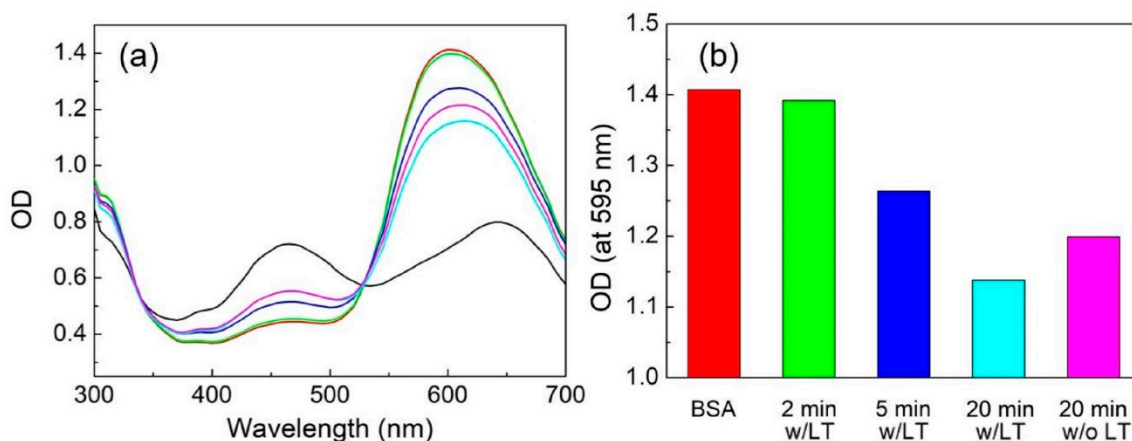


Figure 7. (a) Absorption spectra of BSA during reaction with Coomassie blue (g250) in a liquid medium. BSA was obtained from the reaction with Au/ZnPP electrodes w/LT for 2 (green line), 5 (blue line), and 20 min (light blue line); w/o LT for 20 min (pink line), BSA (red line), and DI water (black line). (b) Optical density (OD) of BSA from (a) at an absorption wavelength of 595 nm.

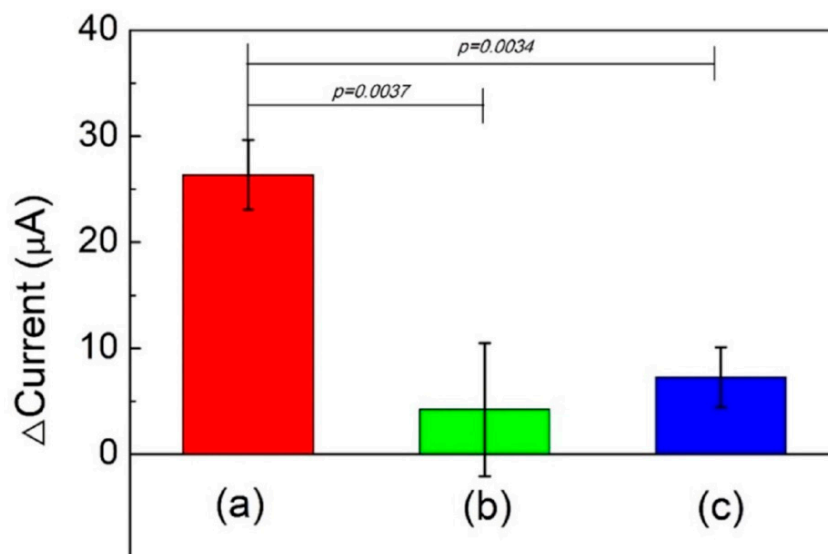


Figure 8. Difference in current between Au/ZnPP and Au/ZnPP/Avastin electrodes (a) w/LT reaction for 10 min, (b) w/o LT reaction for 10 min, and (c) w/o LT reaction for 1.5 h.

3.6. VEGF Detection and Reproducibility, Stability, and Specificity Tests

Figure 9 shows the results of the sensitivity to VEGF of the Au/ZnPP/Avastin/BSA electrodes. VEGF detection by amperometry was conducted using Au/ZnPP/Avastin/BSA electrodes (w/LT and w/o LT). The Au/ZnPP/Avastin/BSA electrode (w/LT) had a linear concentration range and sensitivity of 0.1 pg/mL to 10 ng/mL and 6.52 $\mu\text{A}/\text{Log}(\text{pg}/\text{mL})\text{-cm}^2$, respectively. The Au/ZnPP/Avastin/BSA electrode (w/o LT) had a linear concentration range and sensitivity of 10 pg/mL to 10 ng/mL and 3.15 $\mu\text{A}/\text{Log}(\text{pg}/\text{mL})\text{-cm}^2$, respectively. The results reported in Figure 8 indicate that the Au/ZnPP electrodes (w/LT) have better efficiency and shorter reaction times when immobilizing Avastin, resulting in a higher antibody bond density on the surface of the Au/ZnPP/Avastin electrode and a

wider range for detecting VEGF. Previous studies showed that the cut-off levels of VEGF in the serums of colorectal cancer (Figure 9, orange dotted line), liver cancer (hepatocellular carcinoma) (Figure 9, purple dotted line), and breast cancer (Figure 9, blue dotted line) patients are 459.0, 271.9, and 70.3 pg/mL, respectively [5,39,40]. The Au/ZnPP/Avastin/BSA electrodes developed in this study can detect VEGF concentrations in both healthy and cancer patients. To investigate the reproducibility and the stability of the proposed sensor, the Au/ZnPP/Avastin/BSA electrode (w/LT) was maintained at 4 and 20 °C for different time periods (i.e., 0, 8, 16, 24, 48, and 64 h). The current for each electrode was measured three times ($n = 3$) by amperometry, and three electrodes were used for all experiments. The results are summarized in Table 1. The relative standard deviations (RSDs) for electrodes stored at 4 °C for 8, 16, 24, 48, and 64 h were 6.88, 7.16, 13.16, 8.81, and 14.49, respectively. The RSDs for electrodes stored at 20 °C for 8, 16, 24, 48, and 64 h were 1.00, 0.97, 3.74, 3.89, and 3.89, respectively. Compared with the current initially measured from the electrode (0 h), the mean current was found to initially increase. However, it subsequently decreased in parallel with increasing time periods at both 4 and 20 °C. The calculations of RSD and p values revealed that the mean currents of Au/ZnPP/Avastin/BSA electrodes obtained at different time points at 4 °C were similar to the initial value; however, RSDs were larger when the electrodes were stored at 20 °C. These observations can be explained by the maintenance of the original stereoscopic protein structure at 4 °C—resulting in a current similar to that initially observed. However, when the temperature is increased over 4 °C, the electrode may trap water molecules from the air to form small droplets, ultimately leading to larger current variations. The Au/ZnPP/Avastin/BSA electrodes stored at 20 °C had a mean RSD of 2.70% (<5%) and a p value of 0.14 (>0.05). Taken together, these results indicated that the Au/ZnPP/Avastin/BSA electrode (w/LT) had a very good reproducibility and stability [41,42].

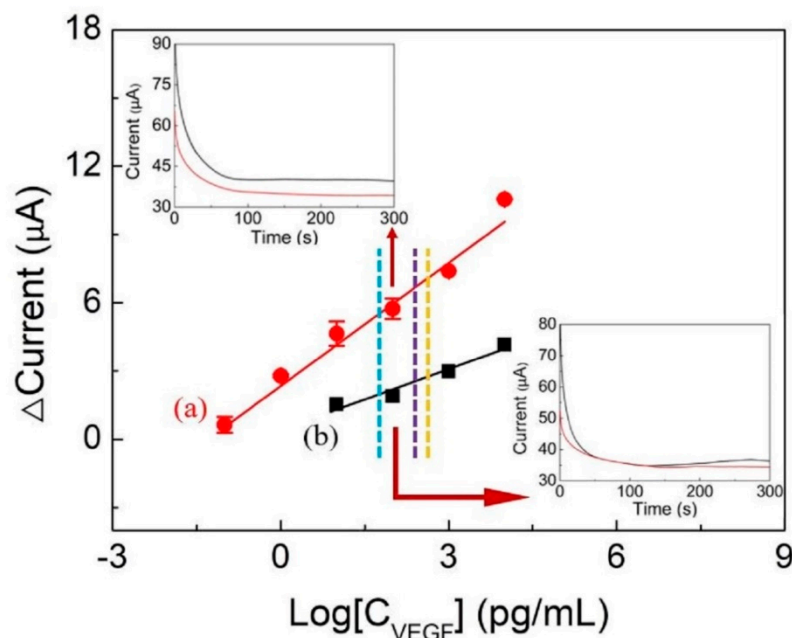


Figure 9. VEGF detection by amperometry using Au/ZnPP/Avastin/BSA electrodes (a) (w/LT) and (b) (w/o LT) in a 20 mM $K_4Fe(CN)_6/K_3Fe(CN)_6$ solution. The blue, purple, and orange dotted lines are cut-off levels for breast [5], liver [39], and colorectal cancers [40], respectively.

Table 1. Statistical analysis of stability test ($n = 3$).

Temperature (°C)	Time (h)	Mean (%)	Standard Deviation (%)	RSD ^a (%)	<i>p</i> Value ^b
4	0	100.00			
	8	105.07	7.23	6.88	0.43
	16	101.29	7.26	7.16	0.82
	24	97.71	12.86	13.16	0.82
	48	95.65	8.43	8.81	0.54
	64	94.57	13.70	14.49	0.63
20	0	100.00			
	8	110.25	1.12	1.00	0.07
	16	102.64	1.01	0.97	0.07
	24	105.52	3.95	3.74	0.19
	48	94.92	3.69	3.89	0.19
	64	94.92	3.69	3.89	0.19

^a RSD (relative standard deviation) = standard deviation/mean \times 100%. ^b *p*-value = independent-sample *t* test with unequal variances (compared to 0 h).

The specificity test of the Au/ZnPP/Avastin/BSA electrode is shown in Figure 10. The results indicated that the electrode has an excellent specificity for VEGF but not other serum components—including HSA, IgG, and creatinine ($p < 0.03$), which are commonly found in human serum and urine. We also investigated the selectivity of the Au/ZnPP/Avastin/BSA electrode for the detection of VEGF through the addition of a mix consisting of human serum albumin and human IgG. The mix had a limited effect on the current ($p = 0.08$), ultimately suggesting that it was unable to significantly affect VEGF detection. Collectively, these results indicated an excellent selectivity of the Au/ZnPP/Avastin/BSA electrode (w/LT) for VEGF.

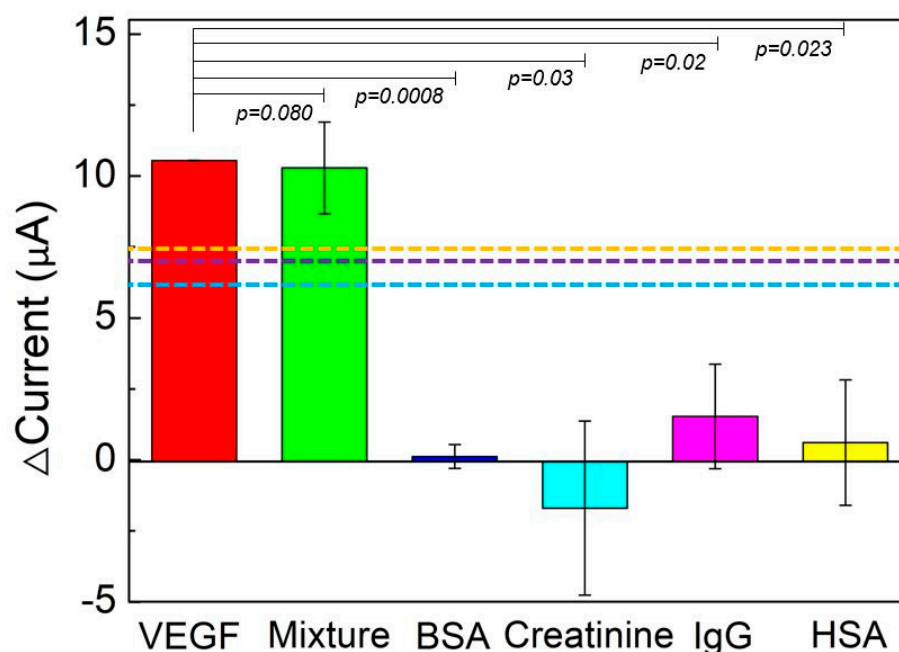


Figure 10. Results of specificity test of Au/ZnPP/Avastin/BSA electrode (w/LT) ($n = 3$). The blue, purple, and orange dotted lines indicate the cut-off levels for breast [5], liver [39], and colorectal cancers [40], respectively.

4. Conclusions

In this work, two Au/ZnPP/Avastin/BSA electrodes (w/LT and w/o LT) were developed as VEGF electrochemical sensors. The linear range to VEGF detection of

the Au/ZnPP/Avastin/BSA electrodes (w/LT) was 0.1 pg/mL–10 ng/mL, while that of Au/ZnPP/Avastin/BSA electrodes (w/o LT) was 10 pg/mL–10 ng/mL. The sensitivity of the Au/ZnPP/Avastin/BSA electrode (w/LT) was 6.52 $\mu\text{A}/\log(\text{pg/mL})\text{-cm}^2$, which is higher than that of the w/o LT electrode (3.15 $\mu\text{A}/\log(\text{pg/mL})\text{-cm}^2$). The Au/ZnPP/Avastin/BSA (w/LT) has good specificity for VEGF, which is hardly influenced by the presence of other molecules, indicating that it has the potential to be applied for in vitro detection of breast cancer, hepatocellular carcinoma, and/or colorectal cancer.

Author Contributions: Conceptualization, H.-Y.L. and M.-Y.H.; methodology, H.-Y.L. and C.-C.L.; validation, H.-Y.L. and C.-C.L.; data curation, M.-Y.H.; writing—original draft preparation; H.-Y.L.; writing—review and editing; M.-Y.H.; visualization, M.-Y.H.; supervision, M.-Y.H.; project administration, M.-Y.H.; funding acquisition, M.-Y.H. All authors have read and agreed to the published version of the manuscript.

Funding: This research was funded by the Ministry of Science and Technology of the Republic of China (MOST 109-2221-E-182-012 and MOST 107-2221-E-182-019-) and by Chang Gung Memorial Hospital and Chang Gung University (BMRP 576).

Acknowledgments: We acknowledge Hung-Wei Yang from the National Sun Yat-sen University for supplying Avastin.

Conflicts of Interest: The authors declare no conflict of interest.

References

1. Smith, K.M. *Comprehensive Coordination Chemistry II*, 3rd ed.; Pergamon Press: Oxford, UK, 2003; pp. 493–506.
2. Bryden, F.; Boyle, R.W. *Advances in Inorganic Chemistry*, 1st ed.; Academic Press: Cambridge, MA, USA, 2016; pp. 141–221.
3. Mashima, T.; Oohora, K.; Hayashi, T. Successive energy transfer within multiple photosensitizers assembled in a hexameric hemoprotein scaffold. *Phys. Chem. Chem. Phys.* **2018**, *20*, 3200–3209. [[CrossRef](#)] [[PubMed](#)]
4. Hennig, G.; Homann, C.; Teksan, I.; Hasbargen, U.; Hasmüller, S.; Holdt, L.M.; Khaled, N.; Sroka, R.; Stauch, T.; Stepp, H.; et al. Non-invasive detection of iron deficiency by fluorescence measurement of erythrocyte zinc protoporphyrin in the lip. *Nat. Commun.* **2016**, *7*, 10776. [[CrossRef](#)] [[PubMed](#)]
5. Broll, R.; Erdmann, H.; Duchrow, M.; Oevermann, E.; Schwandner, O.; Markert, U.; Bruch, H.P.; Windhövel, U. Vascular endothelial growth factor (VEGF)—A valuable serum tumour marker in patients with colorectal cancer? *Eur. J. Surg. Oncol.* **2001**, *27*, 37–42. [[CrossRef](#)] [[PubMed](#)]
6. Ding, C.; Luo, J.; Fan, X.; Li, L.; Li, S.; Wen, K.; Feng, J.; Wu, G. Elevated Gab2 induces tumor growth and angiogenesis in colorectal cancer through upregulating VEGF levels. *J. Exp. Clin. Cancer Res.* **2017**, *36*, 56. [[CrossRef](#)]
7. Kido, S.; Kitadai, Y.; Hattori, N.; Haruma, K.; Kido, T.; Ohta, M.; Tanaka, S.; Yoshihara, M.; Sumii, K.; Ohmoto, Y.; et al. Interleukin 8 and Vascular Endothelial Growth Factor—Prognostic Factors in Human Gastric Carcinomas? *Eur. J. Cancer* **2001**, *37*, 1482–1487. [[CrossRef](#)]
8. Chen, H.C.; Qiu, J.T.; Yang, F.L.; Liu, Y.C.; Chen, M.C.; Tsai, R.Y.; Yang, H.W.; Lin, C.Y.; Lin, C.C.; Wu, T.S.; et al. Magnetic-composite-modified polycrystalline-silicon nanowire field-effect transistor for vascular endothelial growth factor detection and cancer diagnosis. *Anal. Chem.* **2014**, *86*, 9443–9450. [[CrossRef](#)]
9. Yang, H.W.; Tsai, R.Y.; Chen, J.P.; Ju, S.P.; Liao, J.F.; Wei, K.C.; Zou, W.L.; Hua, M.Y. Fabrication of a nano-gold-dot array for rapid and sensitive detection of vascular endothelial growth factor in human serum. *ACS Appl. Mater. Interfaces* **2016**, *8*, 30845–30852. [[CrossRef](#)]
10. Taiwan Cancer Clinic Foundation. Available online: http://www.tccf.org.tw/old/medecine/nm_29.htm (accessed on 10 January 2021).
11. Napoleone, F.; Kenneth, J.H.; William, N.T. Bevacizumab (Avastin), a humanized anti-VEGF monoclonal antibody for cancer therapy. *Biochem. Biophys. Res. Commun.* **2005**, *333*, 328–335. [[CrossRef](#)]
12. Kim, M.; Lezzi, R., Jr.; Shim, B.S.; Martin, D.C. Impedimetric Biosensors for Detecting Vascular Endothelial Growth Factor (VEGF) Based on Poly(3,4-ethylene dioxythiophene) (PEDOT)/Gold Nanoparticle (Au NP) Composites. *Front. Chem.* **2019**, *7*, 234–245. [[CrossRef](#)]
13. Dehghani, S.; Nosrati, R.; Yousefi, M.; Nezami, A.; Soltani, F.; Taghdisi, S.M.; Abnous, K.; Alinolandi, M.; Ramezani, M. Aptamer-based biosensors and nanosensors for the detection of vascularendothelial growth factor (VEGF): A review. *Biosens. Bioelectron.* **2018**, *110*, 23–37. [[CrossRef](#)]
14. Jorge, R.; Costa, R.A.; Calucci, D.; Cintra, L.P.; Scott, I.U. Intravitreal bevacizumab (Avastin) for persistent new vessels in diabetic retinopathy. *Retina* **2006**, *26*, 1006–1013. [[CrossRef](#)] [[PubMed](#)]
15. Yuan, Y.; Hu, T.; Zhong, X.; Zhu, M.; Chai, Y.; Yuan, R. Highly Sensitive Photoelectrochemical Biosensor Based on Quantum Dots Sensitizing Bi₂Te₃ Nanosheets and DNA-Amplifying Strategies. *ACS Appl. Mater. Interfaces* **2020**, *12*, 22624–22629. [[CrossRef](#)]

16. Fan, B.; Fan, Q.; Cui, M.; Wu, T.; Wang, J.; Ma, H.; Wei, Q. Photoelectrochemical Biosensor for Sensitive Detection of Soluble CD44 Based on the Facile Construction of a Poly(ethylene glycol)/Hyaluronic Acid Hybrid Antifouling Interface. *ACS Appl. Mater. Interfaces* **2019**, *11*, 24764–24770. [CrossRef] [PubMed]
17. Gai, P.; Gu, C.; Li, H.; Sun, X.; Li, F. Ultrasensitive Ratiometric Homogeneous Electrochemical MicroRNA Biosensing via Target-Triggered Ru(III) Release and Redox Recycling. *Anal. Chem.* **2017**, *89*, 12293–12298. [CrossRef] [PubMed]
18. Chang, J.; Wang, X.; Wang, J.; Li, H.; Li, F. Nucleic Acid-Functionalized Metal–Organic Framework-Based Homogeneous Electrochemical Biosensor for Simultaneous Detection of Multiple Tumor Biomarkers. *Anal. Chem.* **2019**, *91*, 3604–3610. [CrossRef] [PubMed]
19. Hou, T.; Xu, N.; Wang, W.; Ge, L.; Li, F. Truly Immobilization-Free Diffusivity-Mediated Photoelectrochemical Biosensing Strategy for Facile and Highly Sensitive MicroRNA Assay. *Anal. Chem.* **2018**, *90*, 9591–9597. [CrossRef]
20. Hou, T.; Zhang, L.; Sun, X.; Li, F. Biphasic photoelectrochemical sensing strategy based on in situ formation of CdS quantum dots for highly sensitive detection of acetylcholinesterase activity and inhibition. *Biosens. Bioelectron.* **2016**, *75*, 359–364. [CrossRef]
21. Xiong, E.; Yan, X.; Zhang, X.; Li, Y.; Yang, R.; Meng, L.; Chen, J. A new photoelectrochemical biosensor for ultrasensitive determination of nucleic acids based on a three-stage cascade signal amplification strategy. *Analyst* **2018**, *12*, 2799–2806. [CrossRef]
22. Chen, J.; Liu, Y.; Zhao, G.C. A Novel Photoelectrochemical Biosensor for Tyrosinase and Thrombin Detection. *Sensors* **2016**, *16*, 135. [CrossRef]
23. Zhang, X.; Zhao, Y.; Li, S.; Zhang, S. Photoelectrochemical biosensor for detection of adenosine triphosphate in the extracts of cancer cells. *Chem. Commun.* **2010**, *48*, 9173–9175. [CrossRef]
24. Chen, H.C.; Chen, Y.T.; Tsai, R.Y.; Chen, M.C.; Chen, S.L.; Xiao, M.C.; Chen, C.L.; Hua, M.Y. A sensitive and selective magnetic graphene composite-modified polycrystalline-silicon nanowire field-effect transistor for bladder Cancer diagnosis. *Biosens. Bioelectron.* **2015**, *66*, 198–207. [CrossRef] [PubMed]
25. Jeyachandran, Y.L.; Mielczarski, J.A.; Mielczarski, E.; Rai, B. Efficiency of blocking of non-specific interaction of different proteins by BSA adsorbed on hydrophobic and hydrophilic surfaces. *J. Colloid Interface Sci.* **2010**, *341*, 136–142. [CrossRef] [PubMed]
26. Hideshima, S.; Sato, R.; Inoue, S.; Kuroiwa, S.; Osaka, T. Detection of tumor marker in blood serum using antibody-modified field effect transistor with optimized BSA blocking. *Sens. Actuators B: Chem.* **2012**, *161*, 146–150. [CrossRef]
27. Zhang, Z.; Hu, R.; Liu, Z. Formation of a Porphyrin Monolayer Film by Axial Ligation of Protoporphyrin IX Zinc to an Amino-Terminated Silanized Glass Surface. *Langmuir* **2000**, *16*, 1158–1162. [CrossRef]
28. Science Online. Available online: <https://highscope.ch.ntu.edu.tw/wordpress/?p=58362> (accessed on 10 December 2020).
29. Latunde-Dada, G.O. *Encyclopedia of Food and Health*, 1st ed.; Academic Press: Cambridge, MA, USA, 2016; pp. 452–460.
30. Coates, J. *Encyclopedia of Analytical Chemistry*; Meyers, R.A., Ed.; John Wiley & Sons Ltd.: Chichester, UK, 2000; pp. 10815–10837. [CrossRef]
31. IR Spectrum Table & Chart. Available online: <https://www.sigmaaldrich.com/technical-documents/articles/biology/ir-spectrum-table.html> (accessed on 28 November 2020).
32. Li, L.; Liao, L.; Ding, Y.; Zeng, H. Dithizone-etched CdTe nanoparticles-based fluorescence sensor for the off–on detection of cadmium ion in aqueous media. *RSC Adv.* **2017**, *7*, 10361–10368. [CrossRef]
33. Onoda, A.; Kakikura, Y.; Uematsu, T.; Kuwabata, S.; Hayashi, T. Photocurrent Generation from Hierarchical Zinc-Substituted Hemoprotein Assemblies Immobilized on a Gold Electrode. *Angew. Commun.* **2011**, *51*, 2628–2631. [CrossRef]
34. Onoda, A.; Kakikura, Y.; Hayashi, T. Cathodic photocurrent generation from zinc-substituted cytochrome b₅₆₂ assemblies immobilized on an apocytochrome b₅₆₂-modified gold electrode. *Dalton Trans.* **2013**, *42*, 16102–16107. [CrossRef]
35. Zhang, H.; Ji, J.; Gonzalez, A.A.; Choi, J.H. Tailoring photoelectrochemical properties of semiconducting transition metal dichalcogenide nanolayers with porphyrin functionalization. *J. Mater. Chem. C* **2017**, *5*, 11233–11238. [CrossRef]
36. Walker, J.M. *The Protein Protocols Handbook*, 2nd ed.; Humana Press: Totowa, NJ, USA, 2002; pp. 15–243. [CrossRef]
37. Compton, S.J.; Jones, C.G. Mechanism of dye response and interference in the Bradford protein assay. *Anal. Biochem.* **1985**, *151*, 369–374. [CrossRef]
38. Congdon, R.W.; Muth, G.W.; Splittgerber, A.G. The binding interaction of Coomassie Blue with proteins. *Anal. Biochem.* **1993**, *213*, 407–413. [CrossRef]
39. Hamdy, M.N.; Shaheen, K.Y.; Awad, M.A.; Barakat, E.M.; Shalaby, S.; Gupta, N.; Gupta, V. Vascular endothelial growth factor (VEGF) as a biochemical marker for the diagnosis of hepatocellular carcinoma (HCC). *Clin. Pract.* **2020**, *17*, 1441–1453.
40. Zajkowska, M.; Głażewska, E.K.; Będowska, G.E.; Choraży, P.; Szmikowski, M.; Ławicki, S. Diagnostic Power of Vascular Endothelial Growth Factor and Macrophage Colony-Stimulating Factor in Breast Cancer Patients Based on ROC Analysis. *Mediat. Inflamm.* **2016**, *2016*, 5962946. [CrossRef] [PubMed]
41. Grabowski, B. “*p* < 0.05” Might Not Mean What You Think: American Statistical Association Clarifies P Values. *J. Natl. Cancer Inst.* **2016**, *108*, djw194. [CrossRef]
42. Andrade, C. The P Value and Statistical Significance: Misunderstandings, Explanations, Challenges, and Alternatives. *Indian J. Psychol. Med.* **2019**, *41*, 210–215. [CrossRef] [PubMed]